Mechanical properties of amorphous Li_xSi alloys: a reactive force field study

2013 Modelling Simul. Mater. Sci. Eng. 21 074002

(http://iopscience.iop.org/0965-0393/21/7/074002)

Modelling Simul. Mater. Sci. Eng. **21** (2013) 074002 (15pp) doi:10.1088/0965-0393/21/7/074002

Mechanical properties of amorphous Li_xSi alloys: a reactive force field study

Feifei Fan[1], Shan Huang[1], Hui Yang[2], Muralikrishna Raju[3], Dibakar Datta[4], Vivek B Shenoy[4,5], Adri C T van Duin[3], Sulin Zhang[2] and Ting Zhu[1]

[1] Woodruff School of Mechanical Engineering, Georgia Institute of Technology, Atlanta, GA 30332, USA
[2] Department of Engineering Science and Mechanics, Pennsylvania State University, University Park, PA 16802, USA
[3] Department of Mechanical and Nuclear Engineering, Pennsylvania State University, University Park, PA 16802, USA
[4] School of Engineering, Brown University, Providence, RI 02912, USA
[5] Department of Materials Science and Engineering, University of Pennsylvania, Philadelphia, PA 19104, USA

E-mail: ting.zhu@me.gatech.edu

Received 25 February 2013, in final form 11 September 2013
Published 8 October 2013
Online at stacks.iop.org/MSMSE/21/074002

Abstract

Silicon is a high-capacity anode material for lithium-ion batteries. Electrochemical cycling of Si electrodes usually produces amorphous Li_xSi (a-Li_xSi) alloys at room temperature. Despite intensive investigation of the electrochemical behaviors of a-Li_xSi alloys, their mechanical properties and underlying atomistic mechanisms remain largely unexplored. Here we perform molecular dynamics simulations to characterize the mechanical properties of a-Li_xSi with a newly developed reactive force field (ReaxFF). We compute the yield and fracture strengths of a-Li_xSi alloys under a variety of chemomechanical loading conditions, including the constrained thin-film lithiation, biaxial compression, uniaxial tension and compression. Effects of loading sequence and stress state are investigated to correlate the mechanical responses with the dominant atomic bonding, featuring a transition from the covalent to the metallic glass characteristics with increasing Li concentration. The results provide mechanistic insights for interpreting experiments, understanding properties and designing new experiments on a-Li_xSi alloys, which are essential to the development of durable Si electrodes for high-performance lithium-ion batteries.

(Some figures may appear in colour only in the online journal)

1. Introduction

Silicon is a promising electrode material for next-generation lithium-ion batteries [1–4]. A major challenge to the application of Si electrodes is electrochemically induced mechanical degradation, which can cause capacity fading and limit the cycle life of lithium-ion batteries [5–8]. During electrochemical cycling, Li usually reacts with Si to form amorphous Li_xSi (a-Li_xSi) alloys [9–15]. Despite the intensive electrochemical study of a-Li_xSi, their mechanical properties and associated atomistic mechanisms remain largely unexplored.

Several recent experimental studies have investigated the mechanical properties of a-Li_xSi. Hertzberg *et al* conducted nanoindentation testing on polycrystalline Si thin films at various stages of lithiation [16]. They reported a strong dependence of Young's modulus and hardness on the Li-to-Si ratio. Young's modulus was found to decrease from an initial value of 92 GPa for pure Si to 12 GPa for $Li_{3.75}Si$, and the hardness changed from 5 to 1.5 GPa, correspondingly. Chon *et al* used the curvature measurement technique to determine the yield stress in a lithiated Si thin film [17]. They reported a yield stress of 0.5 GPa for a-$Li_{3.5}Si$, and other thin-film lithiation experiments reported similar values [18]. Kushima *et al* measured the fracture strength and plasticity of lithiated Si nanowires by *in situ* tensile testing inside a transmission electron microscope [19]. The tensile strength decreased from the initial value of about 3.6 GPa for pristine Si nanowires to 0.72 GPa for a-Li_xSi ($x \sim 3.5$) nanowires. They also reported large fracture strains that range from 8% to 16% for a-Li_xSi ($x \sim 3.5$) nanowires, 70% of which remained unrecoverable after fracture.

The mechanical properties of a-Li_xSi alloys have also been studied recently using quantum mechanical and interatomic potential calculations. Shenoy *et al* performed density functional theory (DFT) calculations of the elastic properties of a-Li_xSi alloys [20]. They showed elastic softening with increasing Li concentration. Zhao *et al* conducted DFT calculations for both the biaxial yield stress in a-Li_xSi thin films and the uniaxial yield stress in bulk a-Li_xSi under tension [21]. They found large differences between the characteristic yield stress levels of the two cases. Cui *et al* developed a modified embedded atomic method (MEAM) interatomic potential for Li_xSi alloys [22]. They performed molecular dynamics (MD) simulations of uniaxial tension for bulk a-Li_xSi at 300 K and showed that the yield strength decreased from about 2 GPa for a-LiSi to 0.5 GPa for a-$Li_{3.75}Si$. In addition, quantum mechanical calculations have been performed to study the atomic structures and energetics associated with Li diffusion and reaction in a-Li_xSi alloys [23–31]. The aforementioned modeling studies not only provide valuable insight into the mechanical properties of a-Li_xSi, but also highlight the challenges in understanding the structure–property relationship in a-Li_xSi. Namely, the composition and atomic structure can change drastically during electrochemical cycling of Si electrodes, involving for example the transition from a Li-poor network glass to a Li-rich metallic glass with increasing Li concentration during lithiation [32, 33].

In this work, we employ a newly developed reactive force field (ReaxFF) to study the mechanical properties of a-Li_xSi alloys using MD simulations. This ReaxFF provides accurate predictions of a set of fundamental properties for Li_xSi alloys, such as Li composition-dependent elastic modulus, open-cell voltage and volume expansion, as shown in appendix A. Compared with DFT, the computational efficiency of ReaxFF enables the large-scale MD simulation of a-Li_xSi, which is crucially important for sampling amorphous structures and thus obtaining their statistically meaningful properties. In addition, ReaxFF is capable of describing various bonding environments, essential for improving the chemical accuracy of simulated structures and properties spanning a wide range of Li compositions.

Our ReaxFF-based MD simulations focus on the mechanical properties of a-Li_xSi alloys under different loading modes and stress states. Currently, an effective method of measuring

the mechanical properties of a-Li_xSi is to test the lithiation stress response of a Si thin film on an inactive substrate (e.g. a Cu underlayer on a Si wafer) [17, 34]. Upon electrochemical lithiation, the substrate constrains the volume expansion in the lithiated Si thin film, thus generating a biaxial compressive stress in the film. The film stress can be determined from the substrate curvature change based on Stoney's equation. The lithiation stresses measured from the thin-film experiments have often been taken as the yield strengths of a-Li_xSi alloys in recent literature. To understand these experiments, we raise the following questions: can these thin-film stresses represent well the plastic properties of a-Li_xSi alloys? In other words, does the loading sequence (concurrent versus sequential chemical and mechanical loading) result in different material properties of the same final product? Furthermore, what is the relationship between the yield strength measured from the thin-film experiment during lithiation and that from other mechanical deformations of a-Li_xSi after lithiation, such as biaxial compression, uniaxial tension and compression? With the limited available experimental data, here we address these questions using MD simulations with ReaxFF. The results provide insight into the effects of composition, loading sequence and stress state on the mechanical properties of a-Li_xSi alloys.

2. Methods and results

2.1. Stress generation during thin-film lithiation

We first perform MD simulations to study the stress generation in an a-Si thin film constrained by a substrate during Li insertion. The atomic structure of a-Si is created by melting and quenching of single-crystal Si. To simulate the lithiation response, we take a supercell of a-Si as a representative volume element (RVE) in an a-Si thin film, as schematically shown in figure 1(*a*). This supercell is subjected to periodic boundary conditions. Its size is free to change in the out-of-film direction, but fixed in the plane of the thin film, mimicking an RVE in a thin film constrained by the substrate. We randomly insert 20 Li atoms at a time and then relax the system at 300 K for 10 ps. The Li concentration is approximately uniform in the system, excluding concentration gradient induced stress. This process of insertion and relaxation is repeated until the Li concentration reaches a desired level. The in-plane biaxial stress is calculated after each step of Li insertion and relaxation. The MD simulations show that both the atomic structures and associated stresses are insensitive to the specific scheme of Li insertion, i.e. the number of Li atoms at each insertion and the frequency of insertion.

Figure 1(*b*) shows the atomic structures of pristine a-Si, a partially lithiated phase of a-LiSi, and fully lithiated a-$Li_{3.75}Si$. The starting system of a-Si consists of 432 Si atoms, and the final one of a-$Li_{3.75}Si$ a total of 2052 Li and Si atoms in the supercell. Figure 1(*c*) shows the structural characteristics of both a-Si and a-$Li_{3.75}Si$ in terms of radial distribution function (RDF), angular distribution function (ADF) and ring statistics, with the dominant features consistent with previous quantum calculations [23, 26]. During MD simulations, the volume increase due to Li insertion is mostly accommodated by free expansion in the out-of-film direction. Figure 1(*d*) shows that the a-Li_xSi thin film initially experiences a sharp increase in in-plane biaxial compressive stress with increasing Li concentration. This stage of stressing is dominated by elastic compression, which arises from the geometrical constraint on the supercell that suppresses lithiation induced expansion in the film plane. Biaxial compression reaches a maximum of -6.5 GPa at $x \sim 0.2$, indicative of the onset of plastic yielding. Further lithiation causes a decrease in the magnitude of the film stress, indicating the decrease in yield stress with increasing Li concentration. Such plastic softening can be attributed to the decreasing fraction of strong covalent Si–Si bonds that resist bond switching and ensuing plastic flow [29], as

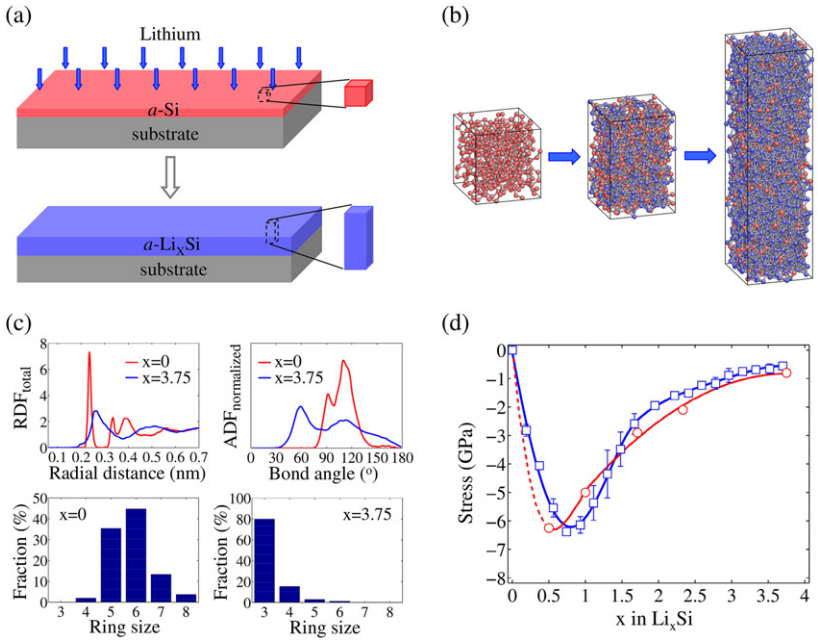

Figure 1. Lithiation of an a-Si thin film constrained by the substrate. (*a*) Schematic of an RVE in the film before and after lithiation. As a result of the in-plane geometrical constraint, this volume element undergoes colossal expansion in the out-of-film direction. (*b*) MD simulated atomic structures of pristine a-Si, a-LiSi and a-$Li_{3.75}Si$, showing the colossal expansion. Red and blue spheres represent Si and Li atoms, respectively. During lithiation, in-plane dimensions of the system remain the same. (*c*) Characterization of atomic structures of a-Si and a-$Li_{3.75}Si$ in terms of RDF, ADF and ring statistics. (*d*) Lithiation-induced biaxial compressive stress in the film as a function of the Li-to-Si ratio, x. Squares represent the MD results, and the blue curve is the numerical fitting. The error bars are due to the results of several configurations at a fixed Li concentration. Circles represent the stresses calculated from an alternative loading mode, i.e. biaxial compression of a lithiated film.

well as the concomitant increase in the weak metallic Li–Li bonds that facilitate plastic flow. Overall, the trend of change of the film stress from MD is similar to that from experimental measurements. However, the magnitude of the MD-simulated compressive film stress is higher at the corresponding Li concentration. For example, the experimentally measured peak value was about -1.9 GPa at $x = 0.2$ [29]. This quantitative difference can be attributed to the short MD simulation time scale that limits the extent of stress relaxation. Nevertheless, MD simulations capture the dominant feature of plastic softening during lithiation.

2.2. Biaxial compression

During the constrained thin-film lithiation, stress is generated owing to the concurrent chemical reaction and mechanical deformation, both of which involve similar atomic processes of bond breaking, switching and reforming. Alternatively, one can evaluate the mechanical properties of a-Li_xSi alloys through chemical lithiation followed by mechanical deformation. That is, a-Si is first lithiated to a specific Li concentration under a stress-free condition, and then is subjected to biaxial compression while keeping the Li concentration fixed. Figure 2(*a*) shows the simulated stress–strain curves of biaxial compression under a strain rate of $5 \times 10^8\ s^{-1}$ at 300 K for several representative Li concentrations. A salient feature in these stress–strain

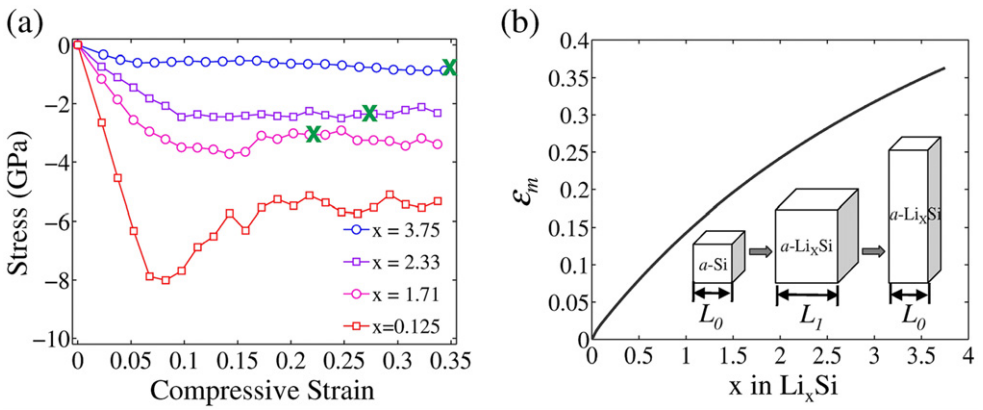

Figure 2. MD simulations of biaxial compression of an RVE of a-Li_xSi alloys. (*a*) Stress–strain curves at four Li concentrations. The green cross symbol indicates the respective yield strengths of σ_Y^m, which correspond to the compression strain, ε_m, specified in (*b*) for each selected concentration. (*b*) Strain–composition curve for a-Li_xSi alloys. The inset describes a sequential loading mode, which consists of a stress-free chemical expansion from a-Si with an initial size of L_0 to a-Li_xSi with a size of L_1, and a biaxial compression on a-Li_xSi under an external compression strain of $\varepsilon_m = (L_1 - L_0)/L_1$, so that a-$Li_xSi$ has the same in-plane dimensions as a-Si.

responses is the yield point phenomenon, featuring the peak stress, load drop and steady flow with limited strain hardening. Notably, the degree of the yield drop varies with Li concentration. In Li-poor phases, the high peak of yield stress is observed with a pronounced load drop. The large peak stress indicates the need of a high load to create enough plastic carriers during the early stage of deformation, a process usually referred to as rejuvenation for creating a deformed amorphous state amenable to plastic flow [35]. In contrast, the yield point phenomenon is less pronounced in the Li-rich phases, which implies the existence of a high fraction of easily flowing components and thus lends a support to constitutive modeling of the Li-rich phase as a visco-plastic solid [6].

Although the detailed atomic processes underlying the yield point phenomenon in a-Li_xSi alloys warrant further study (as demonstrated in appendix B), we focus on extracting the yield strength of σ_Y^m from the above *mechanical* (m) deformation of biaxial compression. The results enable us to correlate σ_Y^m with σ_Y^{cm} evaluated from the thin-film lithiation that involves a concurrent *chemomechanical* (cm) process. Note that in order to determine σ_Y^m at a specific Li concentration from the stress–strain curve, one needs to specify the strain at yielding, as shown in figure 2(*b*). Here we define the compressive strain at yielding as $\varepsilon_m = (L_1 - L_0)/L_1$, where L_1 and L_0, respectively, denote the supercell size of the stress-free a-Li_xSi and the initial a-Si, as schematically shown in the inset of figure 2(*b*). Application of the compressive strain at yielding to a-Li_xSi cancels the in-plane expansion induced by the stress-free lithiation, which is consistent with the boundary condition of rigid in-plane constraints during thin-film lithiation. Given ε_m at a specific Li concentration, we determine the associated compressive yield strength σ_Y^m from the biaxial compressive stress–strain curve in figure 2(*a*). As indicated by the cross symbols in figure 2(*a*), σ_Y^m corresponds to the characteristic plateau stress of plastic flow. To compare σ_Y^m with σ_Y^{cm}, we add in figure 1(*d*) σ_Y^m as a function of Li concentrations (the red solid line). It is seen that the yield strengths of σ_Y^m from biaxial compression are consistent with those of σ_Y^{cm} from thin-film lithiation, by noting that the time scales achievable in MD simulations are similar for the two cases studied. This consistency indicates that the steady-state flow stress during the *mechanical* deformation of an a-Li_xSi alloy can be effectively taken as its yield strength, even under the *chemomechanical* loading condition.

The above yield strengths are at variance with previous atomistic simulation results [21, 22]. The discrepancy arises mainly from the different definitions of yield strength. As shown in figure 2(*a*), the stress–strain curve from MD simulation usually exhibits the yield point phenomenon, which involves a peak stress that is followed by stress drop (i.e. softening) and subsequent steady-state flow at a plateau stress. The value of the yield peak depends sensitively on various factors such as the applied strain rate and temperature, sample preparation (e.g. annealing temperature and rate), as well as the chemical composition of the alloys. The conventional 0.2% offset yield stress, as defined by Cui *et al* [22] in their interatomic potential-based MD simulations, is closely correlated with the yield peak, thus being dependent on the aforementioned factors. On the other hand, stress-controlled energy minimization is performed by Zhao *et al* [21], and the yield strength is defined as the critical stress at the load drop or strain jump, which is also closely correlated with the yield peak. In addition, the first-principles calculations by Zhao *et al* [21] are performed in a small amorphous system with a highly non-uniform atomic structure and thus the results are likely a function of the system size, an effect that has not been studied systematically by Zhao *et al* [21].

In contrast, we define the yield strength as the steady-state flow stress that is less sensitive to the value of the yield peak. More importantly, our definition facilitates a correlation of the yield strength between biaxial deformation and thin-film lithiation. This is because figure 2(*b*) shows that the typical compressive strains during thin-film lithiation are mostly larger than 10%, and hence the steady-state flow stress in biaxial deformation, which prevails at large strains, is more relevant to the yield strength in thin-film lithiation. In addition, the steady-state flow stress obtained in our MD simulations is insensitive to the system size, which ranges from 3 nm × 3 nm × 3 nm (∼2000 atoms) to 6 nm × 6 nm × 6 nm (∼16 000 atoms).

Hertzberg *et al* [16] report the experimental measurements of hardness of a-Li_xSi alloys using the nanoindentation method. Due to the well-known strain rate effects on MD, it is not possible to quantitatively compare MD with experimental results. However, while these measurements represent the first experimental effort to quantify the yield strength of a-Li_xSi alloys, there are several uncontrolled factors in the experiments, such as uncertainty on the spatial distribution of Li considering the recently discovered two-phase mechanism in the first lithiation of a-Si [14, 15], as well as uncertainty on the structural and composition changes when the lithiated samples were transferred to mechanical testing. Hence, well-controlled experimental studies are critically needed in future research.

2.3. Uniaxial tension

In addition to the biaxial compression of a-Li_xSi, we conduct MD studies of uniaxial deformation. The uniaxial tension of a-Li_xSi nanowires is simulated by applying a constant strain rate of $10^8\ s^{-1}$ at 300 K. Figure 3(*a*) shows the tensile stress–strain curves for a Li-poor (a-$Li_{0.125}Si$) and a Li-rich (a-$Li_{3.75}Si$) nanowire, both of which exhibit initially linear and subsequently non-linear responses, followed by a load drop. The linear response corresponds to elastic deformation, with Young's moduli fitted as 65 GPa for a-$Li_{0.125}Si$ and 12 GPa for a-$Li_{3.75}Si$. Evidently, the nanowires undergo elastic softening with increasing Li concentration. This result is indicative of the stiffer bonding of Si–Si than Li–Li, which is consistent with the previous experimental measurements [19] and first-principles calculations [20]. Compared with that of the a-$Li_{0.125}Si$ nanowire, the stress–strain curve of a-$Li_{3.75}Si$ exhibits a considerably larger range of nonlinearity beyond the proportional limit. Such a difference can be ascribed to the existence of an increasing fraction of easily flowing components with increasing Li concentration, an effect that is also responsible for different yield point responses during biaxial compression, as discussed earlier.

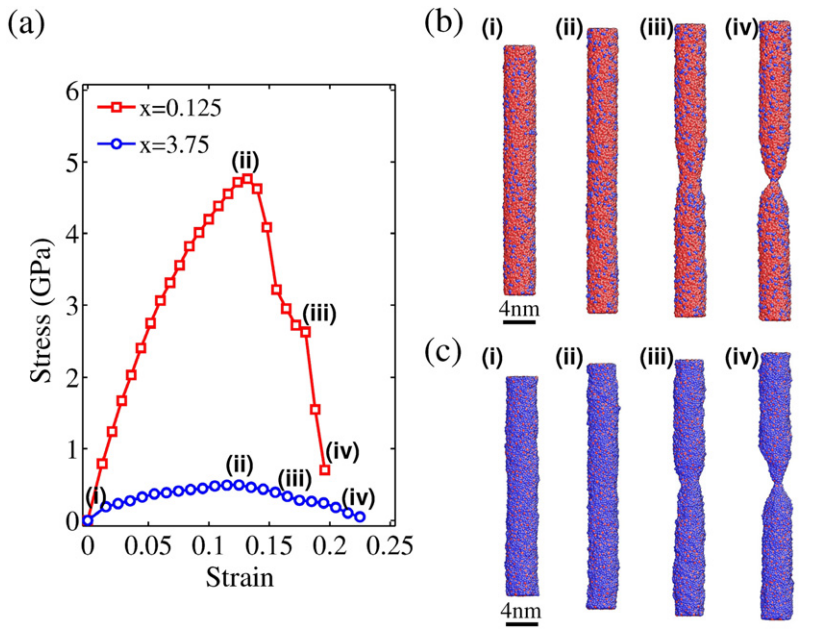

Figure 3. MD simulations of uniaxial tension of a-Li_xSi nanowires. (*a*) Engineering stress–strain curve for both the representative Li-poor (a-$Li_{0.125}$Si) and Li-rich (a-$Li_{3.75}$Si) nanowires. (*b*) Atomic structures of an a-$Li_{0.125}$Si nanowire at the state of (i) zero stress, (ii) maximum stress (before the onset of necking), (iii) severe necking and (iv) fracture. (*c*) Same as (*b*) except for an a-$Li_{3.75}$Si nanowire.

Unique to uniaxial tension, the nanowires are prone to necking instability. It has been previously understood that the onset of necking arises from insufficient strain hardening to compensate for the geometrical softening associated with the reduction of cross-sectional area during tensile elongation [36]. Since the amorphous solid usually lacks strain hardening, as shown earlier in biaxial compression, the neck grows in both a-$Li_{0.125}$Si and a-$Li_{3.75}$Si nanowires (figures 3(*b*) and (*c*)), causing fracture in the necked region. Because the associated load drop prevents an extensive plastic flow, uniaxial tension is not an effective loading mode to study post-yielding behavior. Nevertheless, MD results furnish an estimate of the ultimate tensile strength of 4.7 GPa and 0.5 GPa for a-$Li_{0.125}$Si and a-$Li_{3.75}$Si, respectively. The corresponding failure strains are similarly around 13%. Because of the high strain rate and short relaxation time in MD, the predicted fracture stress and strain of a-$Li_{3.75}$Si nanowires represent the upper limit of experimental results from the tensile testing of lithiated Si nanowires [19, 37]. In addition, we note that the a-$Li_{0.125}$Si nanowire exhibits an abrupt load drop, as opposed to a gradual decrease in a-$Li_{3.75}$Si. This difference in the post-necking response can be attributed to the relatively high elastic stiffness of the a-$Li_{0.125}$Si nanowire, which results in a large elastic energy release to drive a sharp load drop in the fracture process. Our MD simulations further show that the slope of the descending stress–strain curve is sensitive to the applied strain rate, with a faster load drop at a lower strain rate.

2.4. Uniaxial compression

In recent years, nanopillar compression has emerged as an effective means of testing the mechanical properties of small-volume materials [38–41]. Compared with uniaxial tension, it avoids the necking instability and thus enables the study of both yield strengths and

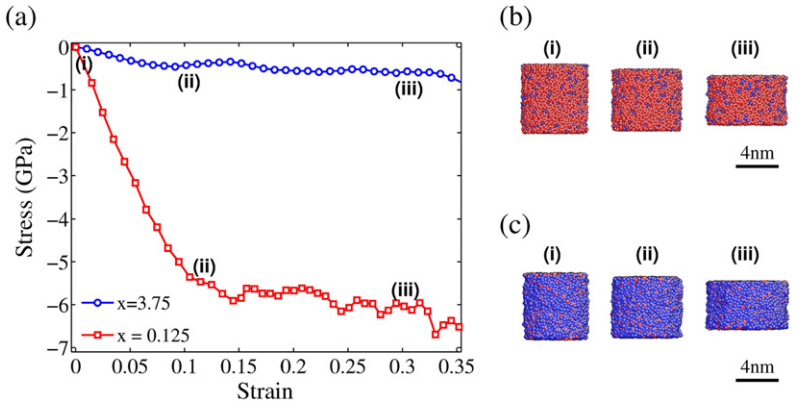

Figure 4. MD simulations of uniaxial compression of a-Li$_x$Si nanopillars. (*a*) Engineering stress–strain curve for both the representative Li-poor (a-Li$_{0.125}$Si) and Li-rich (a-Li$_{3.75}$Si) nanopillars. (*b*) Atomic structure of an a-Li$_{0.125}$Si nanopillar at compressive strains of (i) zero, (ii) 10% and (iii) 30%. (*c*) Atomic structures of an a-Li$_{3.75}$Si nanopillar at compressive strains of (i) zero, (ii) 10% and (iii) 30%.

post-yielding properties. Figure 4(*a*) shows the simulated stress–strain curves of uniaxial compression for a-Li$_{0.125}$Si and a-Li$_{3.75}$Si nanopillars under a strain rate of 5×10^8 s^{-1} at 300 K. Similar to nanowires under uniaxial tension, the compressed nanopillars experience initial elastic deformation. The fitted Young's moduli for a-Li$_{0.125}$Si and a-Li$_{3.75}$Si are consistent with those in tension. Moreover, the magnitude of the flow stress is close to that of the ultimate strength in the tensile testing for both a-Li$_{0.125}$Si and a-Li$_{3.75}$Si.

In contrast to the biaxial compression of an RVE, as shown in figure 2, the yield drop phenomenon disappears in the Li-poor nanopillars of a-Li$_{0.125}$Si under uniaxial compression at 300 K. It has been previously shown that the magnitude of the peak yield stress and the sharpness of the associated load drop in amorphous solids are controlled by the interplay of the annealing rate during sample preparation and the applied strain rate during deformation [35], which, respectively, controls the amount of the pre-existing and deformation-induced plastic flow carriers. However, both the annealing and strain rates are the same in our simulations of biaxial compression and uniaxial compression. The major difference is that the nanopillars have free surface while the RVEs with periodic boundary conditions do not. Hence, we attribute the absence of the yield drop phenomenon in nanopillar compression to the effect of free surface, i.e. a large number of surface dangling bonds enhance plastic flow and thus suppress the yield peak. In addition, the simulated nanopillars experience steady flow (figure 4(*a*)) with a large range of homogeneous compression (figures 4(*b*) and (*c*)), rather than the development of a dominant, localized shear band that would cause premature failure and load drop. This phenomenon can be attributed to the relatively small size of our nanopillars, which effectively prevents shear band formation, a well-recognized sample size effect on deformation in amorphous solids [42]. Finally, we note that the above MD study of uniaxial deformation in terms of free-standing nanowires and nanopillars, instead of RVEs, is motivated by the consideration that these simulations could provide valuable reference and insight for future experiments on a-Li$_x$Si nanowires and nanopillars.

2.5. Biaxial yield surface

Finally, we summarize the simulated results of yield strengths in figure 5 in terms of the biaxial yield surface in the true stress space, in order to provide a unified perspective on the mechanical

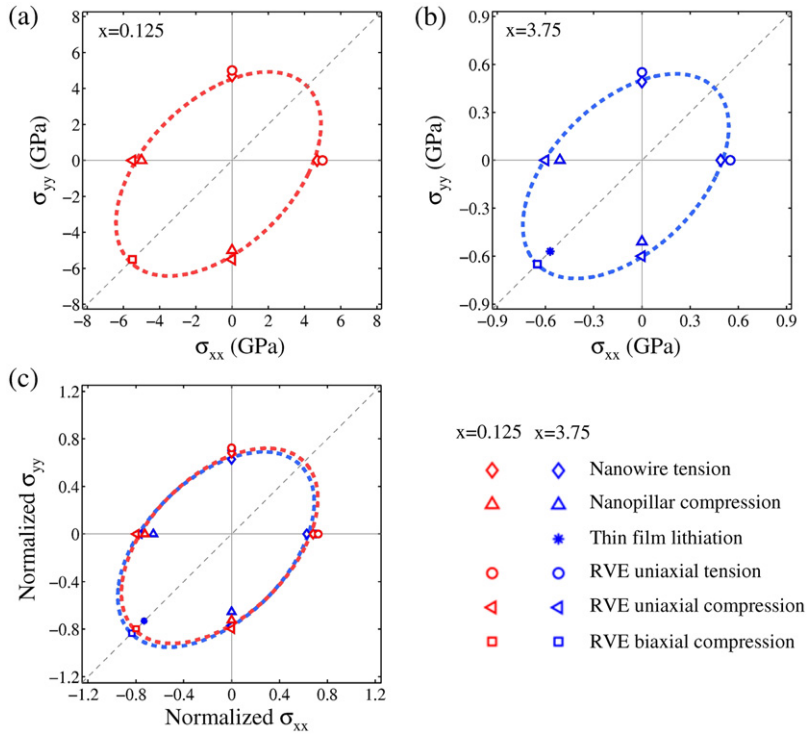

Figure 5. Biaxial yield surface of a-Li_xSi alloys. (*a*) Yield surface in the true stress space for a Li-poor phase of a-$Li_{0.125}Si$ under various loading conditions. The three loading modes on RVEs are performed under a strain rate of $5 \times 10^8\ s^{-1}$ at 300 K. Reflection symmetry is employed to plot the yield surface about the line of $\sigma_{xx} = \sigma_{yy}$, since amorphous solids are isotropic. The dashed line is drawn as a guide to the eye. (*b*) Same as (*a*) except for a Li-rich phase of a-$Li_{3.75}Si$. (*c*) Results in (*a*) and (*b*) are normalized by the respective value of the long radius of the ellipse.

properties of a-Li_xSi alloys. In addition to the yield strengths obtained in sections 2.1–2.4, we include in figure 5 the additional results of flow strengths in uniaxial tension and compression of RVEs. Despite the limited data set, several salient features emerge. First, plastic yielding depends sensitively on Li content. This has been demonstrated through a Li-poor phase of a-$Li_{0.125}Si$ in figure 5(*a*) and a Li-rich phase of a-$Li_{3.75}Si$ in figure 5(*b*). Such a difference arises because the plastic flow characteristics of the former are dominated by strong covalent Si–Si bonds but the latter by weak metallic Li–Li bonds. Second, the asymmetry in tension and compression exists, as seen in uniaxial deformations from figures 5(*a*) and (*b*). Such an asymmetry is a hallmark of amorphous solids [43], manifesting the effect of normal stress on shear strength. It is observed in both Li-poor and Li-rich a-Li_xSi alloys, despite the drastically different structures and bonding characteristics. That is, the directional, covalent network of Si dominates in the former, while the randomly close-packed metallic Li in the latter. The initial yielding behavior in an amorphous material is expected to have a relatively high sensitivity on pressure, since the nucleation of plasticity carriers such as shear transformation zones is usually accompanied by the dilatation of atomic structure. However, our yield strength is defined as the steady-state flow stress at strains greater than 10%, and its pressure dependence can be different from that of the initial yielding. Specifically, when a system is deformed to large strains, it should have already generated a significant amount of plasticity carriers. As a result, the system volume is not necessarily required to change significantly to sustain the

steady-state flow at high strains, such that plastic yielding becomes less sensitive to pressure, as observed in our MD results. Third, the biaxial compression yield strength is a little higher than the uniaxial one, owing to the geometrical confinement effects on plastic deformation. Fourth, figure 5(*c*) shows that the normalized biaxial yield surfaces are similar between the a-$Li_{0.125}Si$ and a-$Li_{3.75}Si$ phases, despite the fact that their dominant atomic bonding characteristics are drastically different. Overall, all the aforementioned features are fundamentally governed by the nature of atomic bonding in a-Li_xSi alloys, and the unique mechanical properties of a-Li_xSi alloys reflect the effective behavior of the mixed covalent and metallic bonds with different fractions and spatial arrangements [19].

3. Conclusions

We have conducted an atomistic study of the mechanical properties of a-Li_xSi alloys with a reactive force field. A variety of chemomechanical deformation processes are simulated by molecular dynamics, including the constrained thin-film lithiation, biaxial compression, uniaxial tension and compression. The results reveal the effects of loading sequence and stress state, which are correlated with the atomic bonding characteristics. Since the a-Li_xSi alloys undergo a large range of change in compositions during electrochemical cycling in lithium-ion batteries, their mechanical behaviors are extremely rich, exhibiting the features of both covalent and metallic amorphous solids [32, 33]. The detailed analyses of the molecular dynamics results in this work provide atomistic insights for understanding the mechanical properties and designing the future testing of lithiated silicon alloys.

Acknowledgments

TZ acknowledges the support of the NSF Grant CMMI-1100205. SZ acknowledges the support of the NSF Grant CMMI-1201058. ACTvD and MR acknowledge the support of the Fluid Interface Reactions, Structures and Transport (FIRST) Center, an Energy Frontier Research Center funded by the US Department of Energy, Office of Science, Office of Basic Energy Sciences. ACTvD and MR were also supported in part by a grant from the US Army Research Laboratory through the Collaborative Research Alliance (CRA) for Multi Scale Multidisciplinary Modeling of Electronic Materials (MSME). The authors thank Dr Yue Qi at General Motors R&D for helpful discussions.

Appendix A. A reactive force field (ReaxFF) for the Li–Si alloy

The parameters of reactive force field (ReaxFF) for Li–Si systems were optimized against a training set from DFT calculations at the B3LYP/6-311G** level, containing a collection of data (energies, geometries, charges, etc). The ReaxFF bond, off-diagonal and valence angle parameters relevant to the Li–Si system were optimized. A total of 10 parameters were fitted to a training set containing 142 data points using a successive single-parameter search method with multiple cycles to account for parameter correlation [44].

The ReaxFF used the Si parameters developed by van Duin *et al* [45] and was further trained to model Li–Si systems. The force field was trained against the equation of states (EOS) for the simple cubic (sc) phases of Si [45] and the body-centered cubic (bcc), face-centered cubic (fcc) and hexagonal-close-packed (hcp) phases of Li. In figure A1, we compare EOS for the bcc, fcc and hcp phases of Li given by ReaxFF and DFT studies. The ReaxFF energy curves are in good agreement with DFT calculations, with a root mean square (rms) deviation

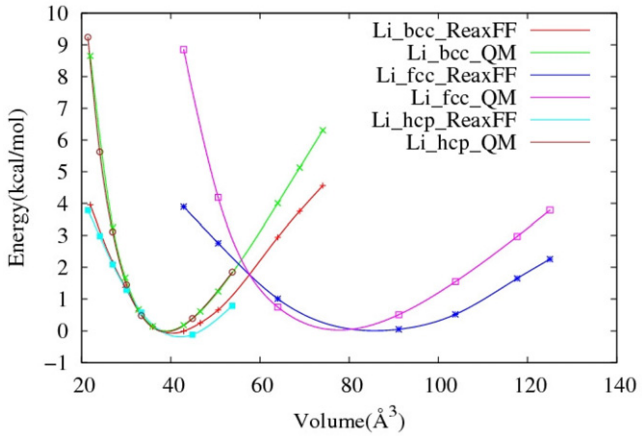

Figure A1. Energy versus volume for the bcc, fcc and hcp phases of pure Li from ReaxFF and DFT calculations.

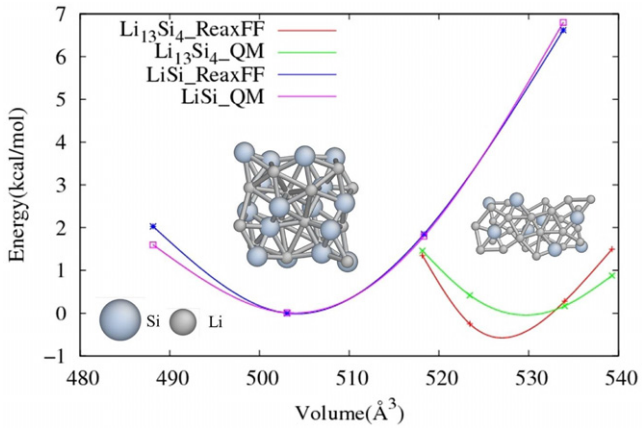

Figure A2. Energy versus volume for crystalline LiSi and $Li_{13}Si_4$ predicted by ReaxFF and DFT calculations.

of only 1.65 kcal mol^{-1} for bcc, 2.14 kcal mol^{-1} for fcc and 2.36 kcal mol^{-1} for hcp phases of Li.

The ReaxFF was also trained against the energy curves for crystalline LiSi, $Li_{12}Si_7$, $Li_{13}Si_4$ and $Li_{15}Si_4$ given by DFT calculations. In figures A2 and A3, we compare the energy curves of LiSi, $Li_{12}Si_7$, $Li_{15}Si_4$ and $Li_{13}Si_4$ crystals predicted by ReaxFF and DFT calculations. The rms deviation of ReaxFF energy curves from DFT calculations is only 0.23 kcal mol^{-1} for LiSi, 9.58 kcal mol^{-1} for $Li_{12}Si_7$, 0.46 kcal mol^{-1} for $Li_{13}Si_4$ and 3.68 kcal mol^{-1} for $Li_{15}Si_4$. Table A1 lists the heat of formation of various Li/Si crystals predicted by ReaxFF and its comparison with corresponding DFT values. The ReaxFF and DFT results are in good agreement.

Using ReaxFF, we evaluate the open-cell voltage [26], volume expansion and Young's modulus of a-Li_xSi as a function of Li concentration, as shown in figure A4. Note that lithiation-induced volume expansion can be affected by the initial structure of a-Si. In our simulations, a-Si is generated by the melting–quenching method, and hence its structure is influenced by the quench rate. Under the simulated quench rate in our MD, a-Si is more

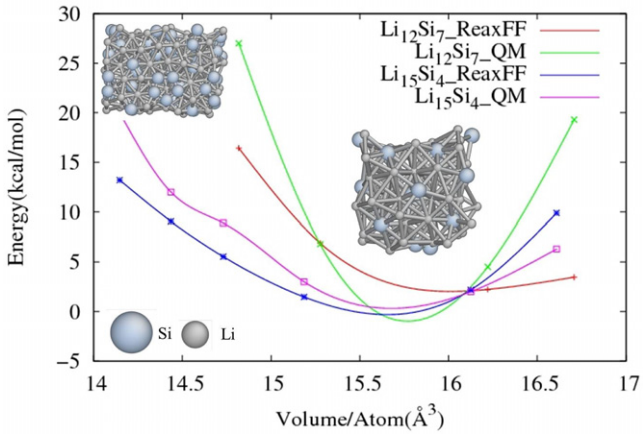

Figure A3. Energy versus volume for crystalline $Li_{12}Si_7$ and $Li_{15}Si_4$ from ReaxFF and DFT calculations.

Table A1. Heat of formation of LiSi, $Li_{13}Si_4$ and $Li_{15}Si_4$ crystals from ReaxFF and DFT calculations.

	ReaxFF (kcal mol^{-1})	DFT (kcal mol^{-1})
LiSi	−14.85	−9.30
$Li_{13}Si_4$	−85.47	−99.75
$Li_{15}Si_4$	−95.02	−104.84

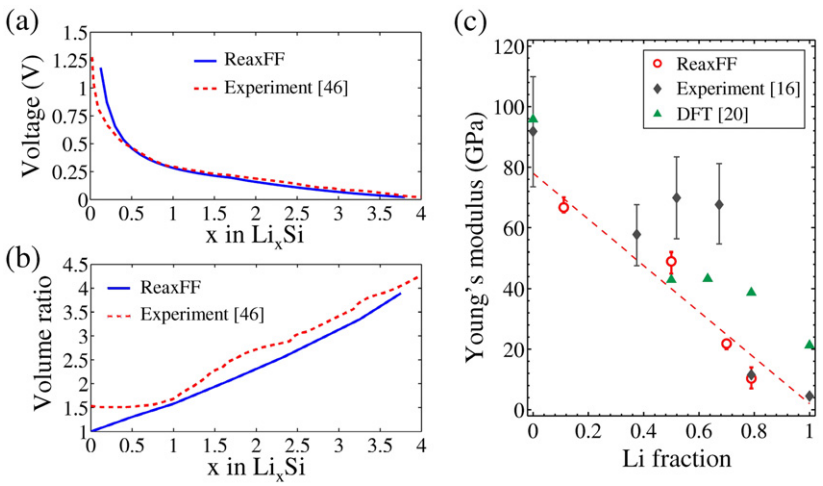

Figure A4. Comparison of properties of a-Li_xSi alloys between experimental measurements and predictions from ReaxFF and DFT. (*a*) Voltage versus Li concentration x. (*b*) Ratio of the current volume and initial volume versus Li concentration x. (*c*) Young's moduli of a-Li_xSi alloys at 300 K.

liquid-like with a mass density of $1.069\rho_0$ (where ρ_0 is the density of c-Si), and contains less free volume to accommodate the Li insertion. In contrast, the a-Si in the experiment (similar to c-Si) usually has a lower density, is more solid-like, and contains more open volume. Therefore, the volume change caused by Li insertion in our simulated a-Si is larger than that for c-Si or

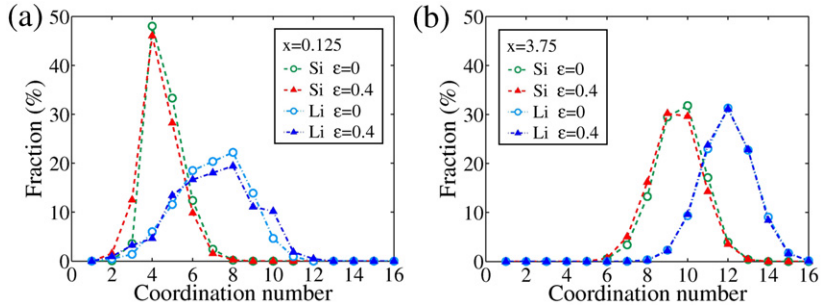

Figure B1. Evolution of atomic coordination numbers under uniaxial tension. (*a*) Distribution of the coordination numbers of Si and Li atoms in a-$Li_{0.125}Si$ at strain values of $\varepsilon = 0$ and 0.4. (*b*) Same as (*a*) except for a-$Li_{3.75}Si$.

experimental a-Si at low Li concentrations [46]. For example, our ReaxFF gives a volume change of 3.7% from c-Si to $Li_{0.125}Si$ by inserting Li atoms to interstitial sites, and 7.0% from as-quenched a-Si to a-$Li_{0.125}Si$.

Despite the aforementioned structure difference, elastic moduli predicted from our simulations show overall agreement with experimental measurements, i.e. a decrease in elastic modulus with increasing Li concentration [16]. However, Young's moduli from the ReaxFF are closer to the rule of mixtures than DFT calculations [20] and experimental measurements [16]. At this moment, the origin of this discrepancy is not clear. While such a discrepancy might arise from the inaccuracy of the ReaxFF, we also note the limitations of other approaches. In experiment, the measured Young's modulus might not correspond to the elastic properties of single-phase Li_xSi when $0 < x < 3.75$. This is because it is unknown whether the Li distribution is uniform or not in partially lithiated samples, considering the two-phase lithiation has been observed in a-Si [14, 15]. In DFT calculations, the results could be limited by the relaxation time and system size, which could compromise the statistical accuracy of the DFT-generated amorphous structures of a-Li_xSi alloys.

Regarding the plastic properties, the previous study shows that the liquid-like a-Si contains a relatively large number of flow defects facilitating plastic deformation [35]. Hence, the yield point phenomenon from our a-Si should be less significant compared with solid-like a-Si, particularly at low Li concentrations. However, we emphasize that the initial structures in all of our simulations, including both the lithiation of thin film and the mechanical loading of a-Li_xSi alloys, are generated using the same protocol of melting–quenching and the resultant structures enable a self-consistent study of how the Li composition affects the mechanical properties of a-Li_xSi alloys. Nevertheless, the effects of different amorphous structures and mass densities on the yield strength of a-Li_xSi alloys warrant a detailed study in the future.

Appendix B. Evolution of atomic structure during mechanical deformation

This paper is focused on the mechanical properties of a-Li_xSi alloys under different loading conditions. In this appendix, we study the atomic-level mechanisms of mechanical relaxation by analyzing the effects of tensile strain and composition on the atomic coordination numbers.

The evolution of atomic coordination numbers during deformation provides basic information on atomistic structural changes under mechanical loading, which can be correlated with dominant bonding characteristics. In figures B1(*a*) and (*b*), we compare the coordination numbers of Si and Li atoms for a-$Li_{0.125}Si$ and a-$Li_{3.75}Si$ alloys under uniaxial tension at

$\varepsilon = 0$ and 0.4, respectively. In both a-$Li_{0.125}Si$ and a-$Li_{3.75}Si$, the number of Si atoms with small coordination numbers increases, and that of Si atoms with large coordination numbers decreases. In addition, the change in the coordination number distribution of Li atoms in a-$Li_{0.125}Si$ is more obvious than that in a-$Li_{3.75}Si$. These results indicate (a) Si–Si and Si–Li bonds break during deformation; (b) in a-$Li_{0.125}Si$, most Li atoms are located in the large open volume of the covalent Si network, and the structural relaxation under high strain occurs mainly through breaking and reforming of covalent Si–Si bonds; (c) in a-$Li_{3.75}Si$, a large fraction of metallic Li atoms and their high mobility facilitate the effective bond switching and reforming to accommodate the imposed mechanical strain.

References

[1] Li H, Huang X J, Chen L Q, Wu Z G and Liang Y 1999 A high capacity nano-Si composite anode material for lithium rechargeable batteries *Electrochem. Solid State Lett.* **2** 547–9

[2] Chan C K, Peng H L, Liu G, McIlwrath K, Zhang X F, Huggins R A and Cui Y 2008 High-performance lithium battery anodes using silicon nanowires *Nature Nanotechnol.* **3** 31–5

[3] Magasinski A, Dixon P, Hertzberg B, Kvit A, Ayala J and Yushin G 2010 High-performance lithium-ion anodes using a hierarchical bottom-up approach *Nature Mater.* **9** 353–8

[4] Liu X H *et al* 2012 *In situ* atomic-scale imaging of electrochemical lithiation in silicon *Nature Nanotechnol.* **7** 749–56

[5] Beaulieu L Y, Eberman K W, Turner R L, Krause L J and Dahn J R 2001 Colossal reversible volume changes in lithium alloys *Electrochem. Solid State Lett.* **4** A137–40

[6] Liu X H *et al* 2011 Anisotropic swelling and fracture of silicon nanowires during lithiation *Nano Lett.* **11** 3312–8

[7] Lee S W, McDowell M T, Berla L A, Nix W D and Cui Y 2012 Fracture of crystalline silicon nanopillars during electrochemical lithium insertion *Proc. Natl Acad. Sci. USA* **109** 4080–5

[8] Liu X H, Zhong L, Huang S, Mao S X, Zhu T and Huang J Y 2012 Size-dependent fracture of silicon nanoparticles during lithiation *ACS Nano* **6** 1522–31

[9] Limthongkul P, Jang Y I, Dudney N J and Chiang Y M 2003 Electrochemically-driven solid-state amorphization in lithium–silicon alloys and implications for lithium storage *Acta Mater.* **51** 1103–13

[10] Obrovac M N and Christensen L 2004 Structural changes in silicon anodes during lithium insertion/extraction *Electrochem. Solid State Lett.* **7** A93–6

[11] Liu X H, Liu Y, Kushima A, Zhang S L, Zhu T, Li J and Huang J Y 2012 *In Situ* TEM experiments of electrochemical lithiation and delithiation of individual nanostructures *Adv. Energy Mater.* **2** 722–41

[12] Yang H *et al* 2012 Orientation-dependent interfacial mobility governs the anisotropic swelling in lithiated silicon nanowires *Nano Lett.* **12** 1953–8

[13] Liu X H, Fan F, Yang H, Zhang S, Huang J Y and Zhu T 2013 Self-limiting lithiation in silicon nanowires *ACS Nano* **7** 1495–503

[14] Wang J W *et al* 2013 Two-phase electrochemical lithiation in amorphous silicon *Nano Lett.* **13** 709–15

[15] McDowell M T, Lee S W, Harris J T, Korgel B A, Wang C, Nix W D and Cui Y 2013 *In Situ* TEM of two-phase lithiation of amorphous silicon nanospheres *Nano Lett.* **13** 758–64

[16] Hertzberg B, Benson J and Yushin G 2011 *Ex-situ* depth-sensing indentation measurements of electrochemically produced Si–Li alloy films *Electrochem. Commun.* **13** 818–21

[17] Chon M J, Sethuraman V A, McCormick A, Srinivasan V and Guduru P R 2011 Real-time measurement of stress and damage evolution during initial lithiation of crystalline silicon *Phys. Rev. Lett.* **107** 045503

[18] Soni S K, Sheldon B W, Xiao X C, Verbrugge M W, Ahn D, Haftbaradaran H and Gao H J 2012 Stress mitigation during the lithiation of patterned amorphous Si islands *J. Electrochem. Soc.* **159** A38–43

[19] Kushima A, Huang J Y and Li J 2012 Quantitative fracture strength and plasticity measurements of lithiated silicon nanowires by *in situ* TEM tensile experiments *ACS Nano* **6** 9425–32

[20] Shenoy V B, Johari P and Qi Y 2010 Elastic softening of amorphous and crystalline Li–Si phases with increasing Li concentration: a first-principles study *J. Power Sources* **195** 6825–30

[21] Zhao K J, Tritsaris G A, Pharr M, Wang W L, Okeke O, Suo Z G, Vlassak J J and Kaxiras E 2012 Reactive flow in silicon electrodes assisted by the insertion of lithium *Nano Lett.* **12** 4397–403

[22] Cui Z W, Gao F, Cui Z H and Qu J M 2012 A second nearest-neighbor embedded atom method interatomic potential for Li–Si alloys *J. Power Sources* **207** 150–9

[23] Chevrier V L and Dahn J R 2009 First principles model of amorphous silicon lithiation *J. Electrochem. Soc.* **156** A454–8

[24] Chevrier V L and Dahn J R 2010 First principles studies of disordered lithiated silicon *J. Electrochem. Soc.* **157** A392–8
[25] Zhang Q F, Zhang W X, Wan W H, Cui Y and Wang E G 2010 Lithium insertion in silicon nanowires: an *ab initio* study *Nano Lett.* **10** 3243–9
[26] Huang S and Zhu T 2011 Atomistic mechanisms of lithium insertion in amorphous silicon *J. Power Sources* **196** 3664–8
[27] Kim H, Chou C Y, Ekerdt J G and Hwang G S 2011 Structure and properties of Li–Si alloys: a first-principles study *J. Phys. Chem.* C **115** 2514–21
[28] Johari P, Qi Y and Shenoy V B 2011 The mixing mechanism during lithiation of Si negative electrode in Li-ion batteries: an *ab initio* molecular dynamics study *Nano Lett.* **11** 5494–500
[29] Zhao K J, Wang W L, Gregoire J, Pharr M, Suo Z G, Vlassak J J and Kaxiras E 2011 Lithium-assisted plastic deformation of silicon electrodes in lithium-ion batteries: a first-principles theoretical study *Nano Lett.* **11** 2962–7
[30] Chan M K Y, Wolverton C and Greeley J P 2012 First principles simulations of the electrochemical lithiation and delithiation of faceted crystalline silicon *J. Am. Chem. Soc.* **134** 14362–74
[31] Jung S C, Choi J W and Han Y K 2012 Anisotropic volume expansion of crystalline silicon during electrochemical lithium insertion: an atomic level rationale *Nano Lett.* **12** 5342–7
[32] Argon A S and Demkowicz M J 2008 What can plasticity of amorphous silicon tell us about plasticity of metallic glasses? *Metall. Mater. Trans.* A **39** 1762–78
[33] Schuh C A, Hufnagel T C and Ramamurty U 2007 Overview No 144—mechanical behavior of amorphous alloys *Acta Mater.* **55** 4067–109
[34] Sethuraman V A, Chon M J, Shimshak M, Srinivasan V and Guduru P R 2010 *In situ* measurements of stress evolution in silicon thin films during electrochemical lithiation and delithiation *J. Power Sources* **195** 5062–6
[35] Demkowicz M J and Argon A S 2004 High-density liquid-like component facilitates plastic flow in a model amorphous silicon system *Phys. Rev. Lett.* **93** 025505
[36] Ashby M F and Jones D R H 2012 *Engineering Materials* vol 1 (Oxford: Butterworth-Heinemann)
[37] Wei Y J, Bower A F and Gao H J 2010 Analytical model and molecular dynamics simulations of the size dependence of flow stress in amorphous intermetallic nanowires at temperatures near the glass transition *Phys. Rev.* B **81** 125402
[38] Uchic M D, Dimiduk D M, Florando J N and Nix W D 2004 Sample dimensions influence strength and crystal plasticity *Science* **305** 986–9
[39] Zhu T, Li J, Ogata S and Yip S 2009 Mechanics of ultra-strength materials *MRS Bull.* **34** 167–72
[40] Zhu T and Li J 2010 Ultra-strength materials *Prog. Mater. Sci.* **55** 710–57
[41] Greer J R and De Hosson J T M 2011 Plasticity in small-sized metallic systems: intrinsic versus extrinsic size effect *Prog. Mater. Sci.* **56** 654–724
[42] Volkert C A, Donohue A and Spaepen F 2008 Effect of sample size on deformation in amorphous metals *J. Appl. Phys.* **103** 083539
[43] Schuh C A and Lund A C 2003 Atomistic basis for the plastic yield criterion of metallic glass *Nature Mater.* **2** 449–52
[44] van Duin A C T, Dasgupta S, Lorant F and Goddard W A 2001 ReaxFF: a reactive force field for hydrocarbons *J. Phys. Chem.* A **105** 9396–409
[45] van Duin A C T, Strachan A, Stewman S, Zhang Q S, Xu X and Goddard W A 2003 ReaxFF(SiO) reactive force field for silicon and silicon oxide systems *J. Phys. Chem.* A **107** 3803–11
[46] Beaulieu L Y, Hatchard T D, Bonakdarpour A, Fleischauer M D and Dahn J R 2003 Reaction of Li with alloy thin films studied by *in situ* AFM *J. Electrochem. Soc.* **150** A1457–64